



# Hydrogen-bonded network in interfacial water confer the catalysts with high formic acid decomposition performance

Nanxing Gao<sup>a,b</sup>, Dongchen Han<sup>a,b</sup>, Tongtong Yang<sup>a,b</sup>, Qinglei Meng<sup>a</sup>, Xian Wang<sup>a,\*</sup>,  
Changpeng Liu<sup>a,b</sup>, Junjie Ge<sup>b,\*</sup>, Wei Xing<sup>a,b,\*\*</sup>

<sup>a</sup> State Key Laboratory of Electroanalytical Chemistry, Laboratory of Advanced Power Sources, Changchun Institute of Applied Chemistry, Chinese Academy of Sciences, Changchun 130022, China

<sup>b</sup> School of Applied Chemistry and Engineering, University of Science and Technology of China, USTC, Hefei 230026, China

## ARTICLE INFO

### Keywords:

Hydrogen-bonded network  
Interfacial water  
Formic acid decomposition

## ABSTRACT

The importance of the dynamic structural evolution of water in the solid–liquid interface cannot be overstated. However, the ubiquitous hydrogen-bonded network is notoriously difficult to probe owing to complex interfacial environment. Formic acid, a fair hydrogen-bond donor and acceptor, is a promising reversible hydrogen storage/release material. Herein, isotope-labeled in-situ mass spectrometry (MS) and *operando* surface-enhanced Fourier transform infrared measurements (*operando* FT-IR) reveal the central role of water during formic acid dehydrogenation. The water-promoted restructured HCOONa-Pd@ANI/C catalyst exhibits 100% selectivity, 100% conversion yield with high stability (even after 112 days) under ambient conditions. Coupled to a proton exchange membrane fuel cell, this integrated system reaches a high power density at 29.81 W·g<sub>Pd</sub><sup>-1</sup>. Our study demonstrates a new pathway involving water, the indispensable proton transfer and exchange through efficiently hydrogen-bonded network in light of *operando* experimental evidence.

## 1. Introduction

Securing decarbonized economies will require efficient production and utilization of green hydrogen at scale. The superior competitiveness and energetic properties (123 MJ kg<sup>-1</sup>) of hydrogen is still restricted owing to the inefficient storage and delivery problems [1]. Formic acid (FA), as a promising liquid organic hydrogen carrier with high volumetric capacity (53 g H<sub>2</sub>/L), enables easy energy storage/transportation process (Table S1) [2–7]. Tracing back to 2008, our research group made the initial discovery that the heterogeneous catalyst Pd-Au/C is capable of promoting formic acid dehydrogenation at room temperature [8]. Meanwhile, formic acid is now readily generated renewably from biomass or CO<sub>2</sub> industrial hydrogenation, and is thereby endowed with a carbon-free feature during the energy cycling [9–12]. Furthermore, combining the high-efficiency hydrogen generator with the proton exchange membrane fuel cells (PEMFCs) is ideally suited for a stable and continuous conversion of green chemical energy to electricity [13–16].

The formic acid decomposition (FAD) reaction is initiated by

activating either the O–H or C–H bond of the HCOOH, with formate (HCOO\*) or carboxyl (COOH\*) formed as intermediate active species on the catalysts surface [17]. It is noted that carbon monoxide is one possible final product in reaction pathway involving COOH\*, however, it is also notorious for its severe poisoning to PEMFCs by blocking the Pt based catalyst surface. Thus, it is crucial and mandatory to explore innovative catalytic materials that could selectively catalyze the FAD via HCOO\* pathway. Palladium, an intriguing element that possesses unique interaction with hydrogen, presents great promise in catalyzing hydrogen production from FAD. While the majority of previous studies were focused on conventional catalyst material engineering, the effect of interfacial H<sub>2</sub>O molecules, which interact closely with the reaction intermediates through hydrogen-bond, was completely ignored, thus leading to incomplete understanding in the FAD reaction.

The unique chemical properties of interfacial water are reckoned to play a key role in various biochemical, energy and catalytic processes [18–21]. Despite the fact that water molecules are interacted with each other through hydrogen bonds, coordination bonds also exist where H<sub>2</sub>O

\* Corresponding authors.

\*\* Corresponding author at: State Key Laboratory of Electroanalytical Chemistry, Laboratory of Advanced Power Sources, Changchun Institute of Applied Chemistry, Chinese Academy of Sciences, Changchun 130022, China.

E-mail addresses: [xwang@ciac.ac.cn](mailto:xwang@ciac.ac.cn) (X. Wang), [gejunjie@ustc.edu.cn](mailto:gejunjie@ustc.edu.cn) (J. Ge), [xingwei@ciac.ac.cn](mailto:xingwei@ciac.ac.cn) (W. Xing).

<https://doi.org/10.1016/j.apcatb.2023.122913>

Received 28 March 2023; Received in revised form 18 May 2023; Accepted 22 May 2023

Available online 22 May 2023

0926-3373/© 2023 Published by Elsevier B.V.

binds to nitrogen (N) or oxygen (O) atoms with free electron pairs. It has been shown that construction of hydrogen-bonded network provides the possibility for orienting intermediates, stabilizing transition states, and lowering the reaction energy barrier. Thanks to a variety of efforts, a wide range of approaches have been applied to characterize the interfacial water interactions and the rapid diffusion of protons through the Grotthuss mechanism [22–24]. Nevertheless, given that the catalytic process typically involves multiple transiently evolved intermediates, how a hydrogen-bonded network forms and performs remains somewhat obscure and require a microscopic and spectroscopic understanding at the molecular level. In case of FAD, water is ubiquitous at practical aqueous/catalyst interfaces as a solvent, while the  $\text{C=O}$  (H-bond acceptor) and  $\text{—OH}$  groups (H-bond donor) in  $\text{HCOOH}$  are expected to be greatly influenced by the hydrogen-bonded network from water.

Inspired by the above insight, here we deliver an in-depth understanding of the central role of interfacial water during formic acid dehydrogenation. The in-situ generated  $\text{Pd@ANI/C}$  catalyst were used for such investigation. *Operando* surface-enhanced FT-IR and in-situ mass spectrometry are adopted to monitor the rapid dynamic changes over the  $\text{Pd@ANI/C}$  catalyst. Remarkably, hydrogen shuttling and exchange due to hydrogen-bond network structure of interfacial water are revealed to play a pivotal role in this process (vide infra). The water-promoted restructured  $\text{HCOONa-Pd@ANI/C}$  catalyst exhibits excellent FAD activity with 100% selectivity, 100% formic acid conversion yield and ultrahigh stability exceeding that of rapidly inactivated commercial  $\text{Pd/C}$ . In tandem with PEMFCs, this integrated system embodies a stable and continuous conversion of green chemical energy to electricity with peak power density at  $29.81 \text{ W} \cdot \text{g}_{\text{Pd}}^{-1}$ . More importantly, isotope-labeled in-situ mass spectrometry further confirmed that water serve as hydrogen source involving in the reaction process through hydrogen bond network. Beyond revealing outstanding catalytic performance for FAD, this work highlights an efficient strategy utilizing interfacial water, which is also attractive for majority catalytic processes.

## 2. Experimental

### 2.1. Chemicals and materials

Aniline ( $\text{C}_6\text{H}_7\text{N}$ , AR, Xilong Chemical Co.), Vulcan carbon powder XC-72 (Cabot Co.),  $\text{PdCl}_2$  (59% Pd, Shanghai Chemical Reagent Co., Ltd), formic acid ( $\text{HCOOH}$ , 99%, Aladdin), sodium formate ( $\text{HCOONa}$ , AR, 99.5%, Aladdin), sodium hydroxide ( $\text{NaOH}$ , ACS  $\geq 98\%$ , Aladdin), hydrochloric acid ( $\text{HCl}$ , AR, Xilong Chemical Co.),  $\text{DCOONa}$  (99.5% D, J&K Scientific Co.),  $\text{D}_2\text{O}$  (99.9% D, J&K Scientific Co.) are obtained commercially and used without further purification. Highly purified argon ( $\geq 99.99\%$ ) is supplied by Changchun Juyang Co Ltd. Ultrapure water ( $18 \text{ M}\Omega \text{ cm}^{-1}$ ) is used to prepare the solutions. 1 g  $\text{PdCl}_2$  is dissolved into 0.1 M  $\text{HCl}$  aqueous solution to obtain  $\text{H}_2\text{PdCl}_4$  solution. All chemicals and materials were obtained from commercial sources without further purification.

### 2.2. Preparation of $\text{Pd@PANI}$

The  $\text{Pd}$ –aniline complex is synthesized by dissolving 15.24 ml of  $\text{H}_2\text{PdCl}_6 \cdot 6 \text{H}_2\text{O}$  in 30 ml of aniline. The solution is stirred for 12 h at room temperature. Then excess aniline is washed out using 0.2 M  $\text{HCl}$  and deionized water for several times. Through this process, a yellow  $\text{Pd}$ –aniline complex powder is obtained after dried at  $55^\circ\text{C}$  overnight.

### 2.3. Preparation of $\text{Pd@PANI/C}$

All syntheses were conducted at room temperature. 258 mg carbon black (Vulcan XC-72) is added into 180 ml ethanol with ultrasound 40 min to get a homogeneous solution. Then 42 mg  $\text{Pd}$ –aniline complex powder is added with stirring for 3 h, to make sure its uniformly dispersed. 0.25 M  $\text{NaOH}$  aqueous solution is added dropwise to adjust

the pH value of the mixture solution, and followed by stirring for 3 h. The  $\text{Pd@PANI/C}$  is filtered and washed with the ultrapure water and then dried at  $55^\circ\text{C}$  overnight.

In order to make the experimental results more comparable, carbon-supported  $\text{Pd}$  without aniline ( $\text{Pd/C}$ ) catalyst is prepared through similar synthetic procedures. The only difference is to replace the precursor  $\text{Pd@PANI}$  with  $\text{H}_2\text{PdCl}_6 \cdot 6 \text{H}_2\text{O}$ .

### 2.4. Preparation of $\text{HCOONa-Pd@PANI/C}$

All syntheses were conducted at room temperature. The obtained  $\text{Pd@PANI/C}$  catalyst is dissolved in 90 ml of deionized water with stirring, followed by the addition of 2.5 ml sodium formate solution (3.6 M). The  $\text{HCOONa-Pd@ANI/C}$  catalyst is collected after 24 h stirring and washing with deionized water until the pH of the filtrate become neutral.

### 2.5. Catalyst characterization

The transmission electron microscopy (TEM) and high resolution transmission electron microscopy (HRTEM), high-annular darkfield scanning transmission electron microscopy (STEM) and element mapping analysis are conducted on Philips TECNAI G2 electron microscope with an acceleration voltage of 200 kV. X-ray diffraction (XRD) measurements are performed with Bruker D8 Advance with  $\text{Cu K}\alpha$  ( $\lambda = 1.5405 \text{ \AA}$ ) as a radiation source. X-ray photoelectron spectroscopy (XPS) are carried out on Kratos AXIS ULTRADLD spectrometer with  $\text{MgK}\alpha$  radiation source. Inductively Coupled Plasma Optical Emission Spectrometry (ICP-OES, USA Thermo Scientific Icap6300) is used to analysis chemical component of the catalyst. UV–Vis spectrum is measured on a Agilent Cary 4000 ultraviolet spectrophotometer. The Fourier transform infrared (FTIR) Spectra were recorded with a Bruker Vertex 70 RTIR spectrometer.

### 2.6. Evaluation of FAD performance

Generally, 120 mg catalyst is added to a round flask with high purified  $\text{N}_2$  blowing for 10 min to remove air. Subsequently, 2.5 ml reaction solution (3.6 M  $\text{HCOOH}$  and 3.6 M  $\text{HCOONa}$ ) is added into the flask with magnetic stirring (400 rpm). The temperature of the whole reaction system is maintained at 303 K by water bath and the released gas was measured volumetrically by the M-Gas Mass Flow Meters from Alicat Scientific and recorded every second by a computer.

The cyclic testing of the catalyst is carried out as follows: after each cycle, the catalyst is washed with deionized water and collected by centrifugation for the next time.

### 2.7. In situ mass measurements

In situ mass spectrometric (MS) measurements are provided by Linglu Instruments (Shanghai) Co. Ltd to detect the production during the FAD process. This test system ensures fast transport of species formed at the catalyst surface to the mass spectrometric compartment, where the volatile products are evaporated into the vacuum system of the mass spectrometer (time constant, ca. 1 s). In a typical test, 0.5 ml of deionized water and 1 mg catalyst are added to the test cell, turn on the mass spectrometer and run it for a while to level off the signal. Subsequently, 0.5 ml of  $\text{HCOONa}$  (3.6 M) is added to the electrolytic cell, so that the concentration of  $\text{HCOONa}$  in the solution after mixing is 1.8 M. Record the addition time of  $\text{HCOONa}$  solution and observe the signal fluctuation in the mass spectrometer after that. Isotope labeling experiments are also performed in the same way, but the corresponding solution is replaced.

## 2.8. Operando surface-enhanced FT-IR measurements

These experiments are conducted in an elevated-pressure cell (Harrick DRK-4-BR4) with a Fourier transform infrared spectrometer (Thermo Scientific Nicolet iS50). The catalysts are dispersed on the gold sheet with surface roughness. Prior to the measurement, vacuum treatment for 30 min is essential to exhaust all gases in the reaction chamber. The background spectrum at 0 min is obtained after the catalyst was treated with a flowing  $N_2$  (1 bar) for 30 min at 30 °C. Subsequently, 1 bar of  $N_2$  are allowed to bubble in sodium formate solution (3.6 M), and flow into the reaction chamber at 30 °C. The spectra are obtained by applying an average of 128 scans with a spectral resolution of 4  $cm^{-1}$ .

## 2.9. Quasi in situ Raman measurements

The Raman measurements are carried out on a confocal microscope Raman system (HORIBA XploRA). A He-Ne laser with 633 nm excitation wavelength and a 50 × microscope objective with a numerical aperture of 0.55 were used in all measurements. Raman frequency was calibrated by a Si wafer during each experiment. Quasi in situ Raman experiments were employed in a homemade Raman cell. The Raman spectral signals at the same location of catalyst are recorded at intervals from the addition of the reaction solution.

## 3. Results and discussion

### 3.1. Catalysts synthesis approaches

The pre-catalyst Pd@ANI/C were fabricated via an aniline monomer interface assembly strategy. In a typical synthesis,  $d,\pi$ -conjugated complex Pd@ANI is initially synthesized via stirring at room temperature (Fig. 1c and S1). The X-ray diffraction analysis and Fourier transform infrared absorption spectrum verify that aniline-derived Pd complex is successfully assembled with its characteristic peaks (Fig. S2)

[25–27]. Sequentially, Pd@ANI are uniformly dispersed onto commercial carbon Vulcan XC-72 with hexagonal shaped crystals disappeared. Appropriate amount of sodium hydroxide is then added to achieve ligand substitution of  $PdCl_4^{2-}$  and deprotonated of the complex (details are described in experimental section). In addition, sodium formate (SF) treated ( $HCOONa$ -Pd@ANI/C) catalyst and carbon-supported Pd without aniline (Pd/C) catalyst are prepared through similar synthetic procedures for comparison and analysis. Inductively coupled plasma atomic emission spectroscopy (ICP-AES) analysis confirm that all the samples possess similar total Pd loading amounts (Table S2).

To further gain insights into the mechanism of the process, we monitor the color changes of the ethanol solution of Pd@ANI under the same conditions. As shown in Fig. 1a, the dissolution of Pd@ANI in ethanol forms a yellow solution, whose color progressively changes to orange-brown within 20 min with the treatment of NaOH. Whereas no obvious changes of the Pd@ANI ethanol solution can be found if only stirring for 20 min. These results imply that the hydroxyl group in NaOH coordinated with palladium via ligand exchanging with chloride. The X-ray photoelectron spectroscopy (XPS) spectrums also indicate the absence of Cl as a result of NaOH treatment (Fig. S3). Notably, only after the addition of sodium formate and water does the mixed solution turns black (Fig. S4). Such phenomena can be attributed to the formation of ultrafine palladium nanoparticles, which will be explored in detail as follows. Typical absorption bands of  $H_2PdCl_4$  solution in ultra-violet-visible (UV-vis) spectrum, located at around 218, 244 and 324 nm, are assigned to ligand-to-metal charge transfer transition (LMCT). [28–30] The absorption band at 430 nm is assigned to a spin-forbidden d–d transition ( $^1A_{2g} \leftarrow ^1A_{1g}$ ) that reflected the square-planar configuration  $Pd^{2+}$  complexes. [31] Significant shift of LMCT absorption bands can be observed when aniline is mixed with  $H_2PdCl_4$  to form Pd@ANI or with the addition of NaOH further (Fig. 1b), confirming that the color change of solution involves the ligand substitution of  $Pd^{2+}$  complexes. In contrast, followed by subsequent sodium formate aqueous solution treatment, the mixture shows typical

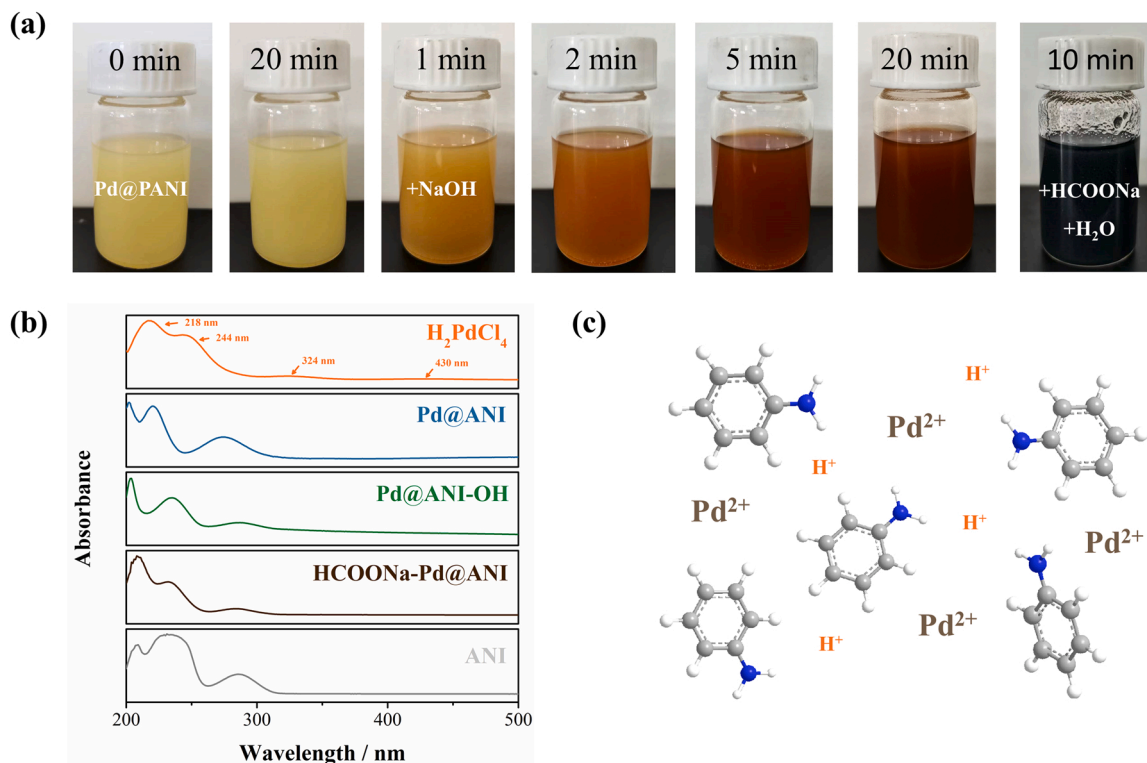


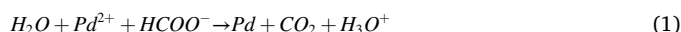
**Fig. 1.** (a) Time-progression color changes of the ethanol solutions of Pd@ANI under different conditions for monitoring the formation of Pd NPs; (b) UV-vis spectrum of the corresponding reaction solution; (c) Schematic representation of Pd@ANI structure.

absorption bands similar to those of aniline monomer. Beyond that, the disappearance of  $\text{Pd}^{2+}$  d-d transition band in the range of 350–600 nm (Fig. S5) further demonstrates the reduction of  $\text{Pd}^{2+}$  to  $\text{Pd}^0$  as expected.

### 3.2. Incremental hydrogen production performance

The catalytic properties of various catalysts are investigated towards FAD at room temperature (Fig. 2a). Remarkably, the catalyst  $\text{Pd@ANI/C}$  performs incremental activity during an induction phase in the FA-SF aqueous solution (FA:SF = 1:1,  $n\text{Pd}/n\text{FA}$  = 0.006). This distinct experimental phenomenon essentially represents an in-situ restructuring process. More interestingly, the  $\text{HCOONa-Pd@ANI/C}$  catalyst, with SF aqueous solution pretreated for restructuring, displays significantly enhanced catalytic performance. This catalyst demonstrates much superior FAD activity (Table S3), with 100% conversion of 9 mmol FA into  $\text{H}_2$  achieved at room temperature within 13 min, in great contrast with the fast inactivation of the  $\text{Pd/C}$  catalyst. Moreover, the results of in-situ mass spectrum measurement and gas chromatograph measurement (Fig. S6) confirm the 100% selectivity of  $\text{HCOONa-Pd@ANI/C}$  catalyst, with the generated gas consists of only  $\text{H}_2$  and  $\text{CO}_2$  and no trace of CO. As shown in Fig. 2b, the cycling performance of  $\text{HCOONa-Pd@ANI/C}$  catalyst is conducted to evaluate the catalytic stability. This catalyst maintains 100% conversion and selectivity in each run, with performance only slightly decreased upon cycling. The 112-days long-term stability experiment (Fig. S7) further confirms the acceptable stability of  $\text{HCOONa-Pd@ANI/C}$  catalyst, which is promising in practical applications of hydrogen production. By utilizing this hydrogen generation unit in tandem with a proton exchange membrane fuel cell, a stable and continuous conversion of green chemical energy to electricity is obtained with power output at  $29.81 \text{ W} \cdot \text{g}_{\text{Pd}}^{-1}$  (Fig. S8).

Given the surface sensitivity of XPS, identification of the valence states of palladium can reveal the chemical changes upon restructuring process. The binding energy value of 343.0 eV ( $\text{Pd } 3d \ 3/2$ ) and 337.7 eV ( $\text{Pd } 3d \ 5/2$ ) of the  $\text{Pd@ANI/C}$  before reaction indicate the existence of palladium as  $\text{Pd}^{2+}$  on the catalyst surfaces (Fig. 2c). [32,33] With water-assisted protons capturing and transferring, sodium formate reduces  $\text{Pd}^{2+}$  to  $\text{Pd}^0$ , accompanied with the release of carbon dioxide (Eq. 1). The in-situ restructuring procedure is schematically illustrated in Fig. 2d. Accordingly, the coexistence of  $\text{Pd}^0$  and  $\text{Pd}^{2+}$  at the  $\text{HCOONa-Pd@ANI/C}$  catalyst surfaces can be observed with the appearance of  $\text{Pd}^0$  peaks centered at 341 eV ( $\text{Pd } 3d \ 3/2$ ) and 335.8 eV ( $\text{Pd } 3d \ 5/2$ ). Beyond that, the absence of  $\text{Pd}^0 \ 3d \ 3/2$  and  $3d \ 5/2$  signals without  $\text{H}_2\text{O}$  addition corroborated that both water and sodium formate are indispensable for this process (Fig. 2c and Fig. S9). To further verify this perception, *operando* mass spectrometry is carried out to monitor the FAD process. An obviously increased mass signal of  $\text{CO}_2$  ( $m/z = 44$ ) is firstly noticed in the initial restructuring period (Fig. 2e). Then sequentially to the  $\text{H}_2$  ( $m/z = 2$ ) product signal appears, which can be attributed to formic acid dehydrogenation reaction. The phenomenon that  $\text{CO}_2$  signal is detected prior to  $\text{H}_2$  provides more compelling evidence for water-promoted restructuring process, in accord with the incremental catalytic performance.



### 3.3. Structural characterization of catalysts

To unambiguously observe the Pd species, the aberration-correction high-angle annular dark-field scanning transmission electron microscopy (AC-HAADF-STEM) imaging technique is employed to

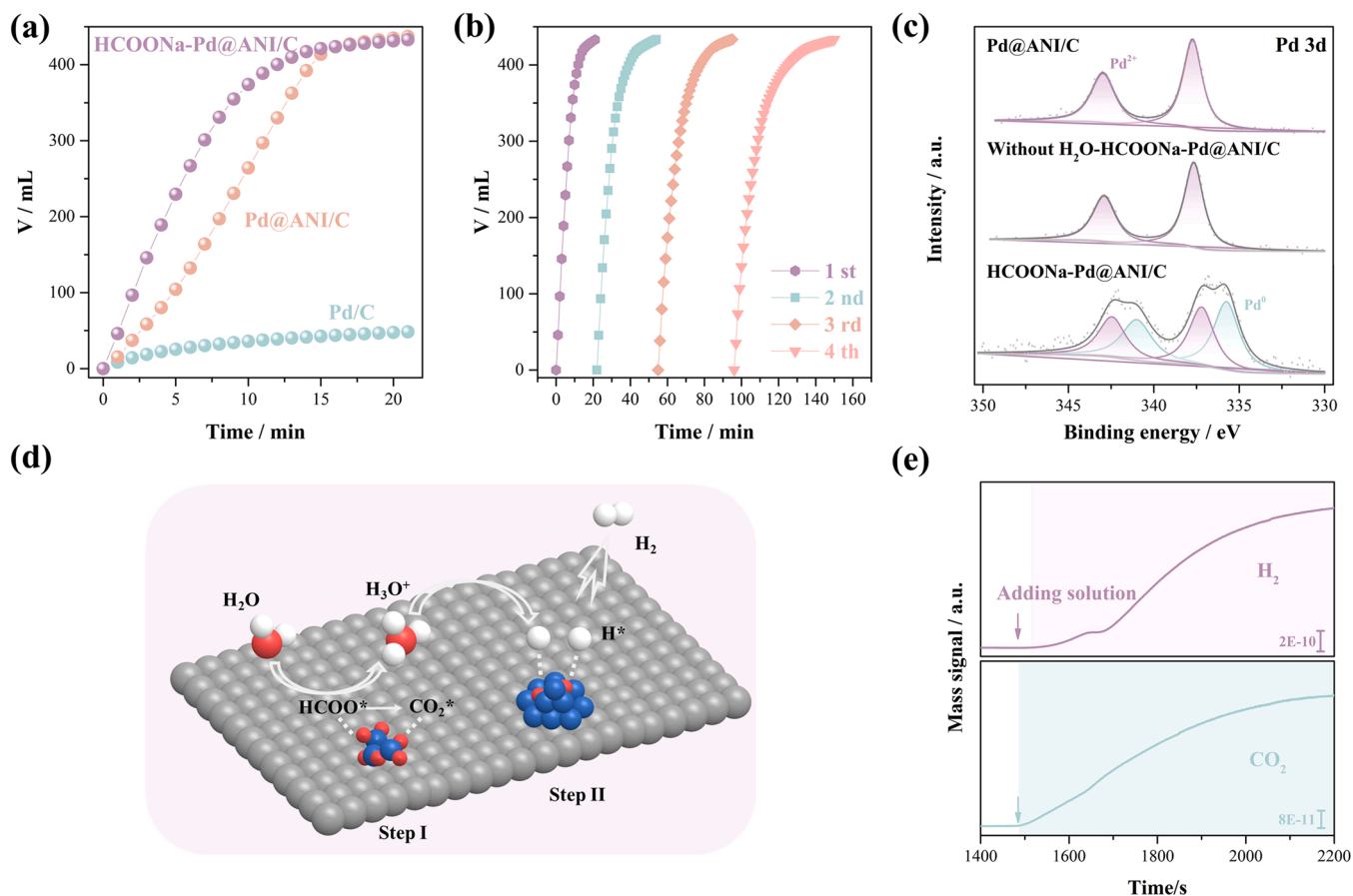


**Fig. 2.** Evaluation of formic acid dehydrogenation activity (a) and stability (b) at 30 °C; (c) Pd 3d XPS spectra of various catalysts; (d) Schematic diagrams illustrating the in-situ restructuring procedure; (e) *Operando* mass monitoring shows the signals of the FAD gaseous products.



distinguish Pd atom based on the difference in Z-contrast. The randomly enlarged image highlights the coexistence of Pd isolated species and clusters in Pd@ANI/C (Fig. 3a and Fig. S10). Blue boxes and yellow circles indicate the dispersed palladium clusters and single Pd atoms, respectively. The geometry of palladium clusters exhibits atomic-layered ensembles with only a few atoms in Pd@ANI/C. Due to Gibbs-Thomson effect, the chemical potential of a spherical nanoparticles with radius  $r$  increases proportional to  $1/r$  [34]. Accordingly, smaller than 2 nm-sized Pd clusters are thermodynamically unstable, so that they tend to form Pd-O bonding at the surface in order to lower the surface free energy, which in turn provides a possible interpretation for existence of palladium as  $\text{Pd}^{2+}$  on the catalyst surface, consistent with the abovementioned XPS analyses.

For  $\text{HCOONa-Pd@ANI/C}$ , palladium nanoparticles with increased average size and ordered crystalline structures are confirmed (Fig. 3c,e and Fig. S11). Intriguingly, from the large-scale scanning transmission electron microscopy (STEM) images, a large number of nanoparticles emerge on the smooth surface of carbon as compared to Pd@ANI/C (Fig. 3b,d). Meanwhile, the density of Pd isolated species significantly decreased. In line with the perception mentioned above, with the assistance of water, sodium formate reduces  $\text{Pd}^{2+}$  to  $\text{Pd}^0$  and ultrafine Pd nanoparticles form through this restructuring process. Notably, the lattice fringes spacing of 0.197 nm on individual Pd nanoparticle (Fig. 3e) is slightly larger than (200) planes lattice spacing (0.195 nm) of the standard face-centered cubic Pd (JCPDS no. 46-1043), which might be attributed to the H-doping into the Pd lattices (i.e., formation of PdH). Energy-dispersive X-ray spectroscopy (EDX) mapping images (Fig. 3f) show that Pd nanoparticles are distributed on the carbon covered with N-rich layers as expected. The static size distribution analysis gives a lateral size distribution of 1–3 nm for Pd nanoparticles (Fig. S12), which is the ideal size for catalytic reactions.

#### 3.4. In-situ spectroscopy to understand the role of $\text{H}_2\text{O}$

To identify the reaction intermediates during in-situ restructuring procedure, *operando* surface-enhanced FT-IR measurements are conducted on Pd@ANI/C catalyst under the reaction condition (Fig. 4a). Prior to the measurement, vacuum treatment for 30 min is essential to exhaust all gases in the reaction chamber. The background spectrum at 0 min is obtained after the catalyst was treated with a flowing  $\text{N}_2$  (1 bar) for 30 min at 30 °C. Subsequently, 1 bar of  $\text{N}_2$  are allowed to bubble in sodium formate solution (3.6 M), and flow into the reaction chamber at 30 °C. As the reaction proceed, the new bands at 2997, 1523, and 1446  $\text{cm}^{-1}$  arise from the stretching vibration of C-H, and the asymmetrical/symmetrical stretching vibration of COO are observed [35,36]. These characteristic peaks are attributed to adsorbed  $\text{HCOO}^*$  species, which are regarded as vital intermediates during formic dehydrogenation to  $\text{H}_2$ . Significantly, the sharp peak at 1616  $\text{cm}^{-1}$  and a broad peak at 3150–3700  $\text{cm}^{-1}$  are assigned to H–O–H bending vibrations and O–H stretching of interfacial water, respectively [37,38]. Besides, the peaks at 2314 and 2375  $\text{cm}^{-1}$  are corresponded to physical adsorbed  $\text{CO}_2^*$  species [39–41].

On basis of the variation of normalized infrared peaks intensity, we monitor the rapid dynamic changes of surface reaction intermediates over the catalyst (Fig. 4b). During the reaction process, the characteristic peak value of  $\text{HCOO}^*$ ,  $\text{H}_2\text{O}^*$  and  $\text{CO}_2^*$  species all increased firstly and then gradually decreased to maintain a steady level (Fig. 4b and Fig. S12). This subtle phenomenon suggests that the water-assisted in-situ restructuring process is completed rapidly within 10 min of the initial reaction. More importantly, it is identified that both water and sodium formate are indispensable as the active intermediate displayed in Eq. 1. The absence of CO infrared peaks (around 1850 or 2120  $\text{cm}^{-1}$ ) further demonstrates the remarkable selectivity of this catalyst during

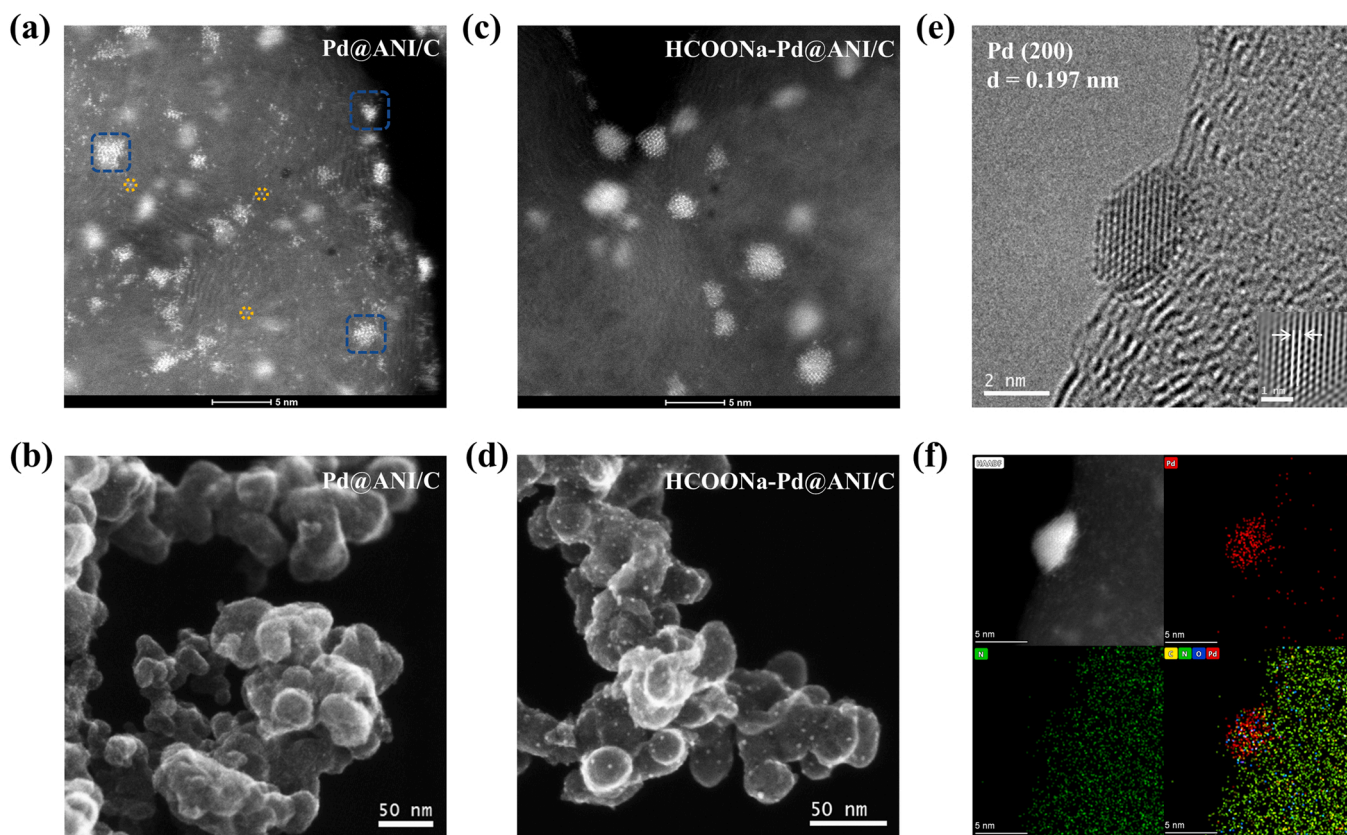


**Fig. 3.** AC-HAADF-STEM and large-scale STEM images of Pd@ANI/C (a,b) and HCOONa-Pd@ANI/C (c,d); (e) High-resolution transmission electron microscopic (HRTEM) image of HCOONa-Pd@ANI/C (insert: zoomed-in fast inverse Fourier transform image to measure lattice fringes spacing) (f) High-angle annular dark-field (HAADF) STEM images and elemental mapping of individual Pd nanoparticle of HCOONa-Pd@ANI/C.

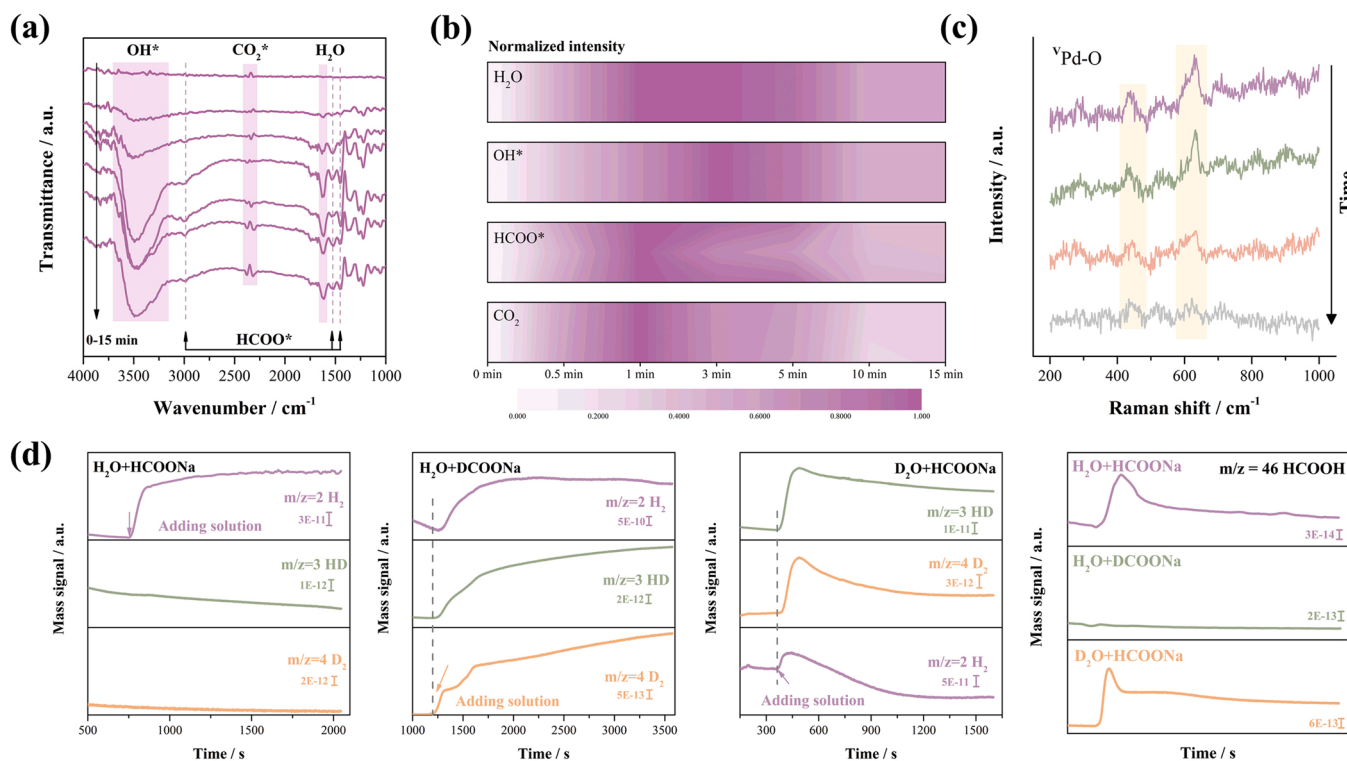


**Fig. 4.** (a) *Operando* surface-enhanced FT-IR spectra for Pd@ANI/C during the treatment of sodium formate solution; (b) Normalized intensity of the corresponding peaks of various adsorbed species; (c) The time-resolved in-situ Raman spectra over Pd@ANI/C with sodium formate solution addition; (d) In-situ MS measurements of H<sub>2</sub> ( $m/z = 2$ ), HD ( $m/z = 3$ ), D<sub>2</sub> ( $m/z = 4$ ) and HCOOH ( $m/z = 46$ ) signals.

FAD process [42,43]. Qualitative analysis of the Pd sites' coordination structure during the restructuring process is realized by quasi in-situ Raman measurements, focusing on the revealing of the dynamic structural evolution. Correspondingly, the characteristic Pd–O stretching vibrations Raman peaks (434 and 633 cm<sup>-1</sup>) gradually disappeared [44, 45], indicating that Pd<sup>2+</sup> is successfully converted to Pd<sup>0</sup> during chemical reduction (Fig. 4c). All these analyses mentioned above further confirm the rationality of proposed reconstruction mechanism, which contributes to the catalyst's superior FAD performance.

Inspired by the water-assisted in-situ restructuring process, we wonder that whether interfacial water also play a key role in the FAD reaction process. Isotope-labeled in-situ mass spectrometry is employed to shed light on the underlying mechanism for the roles of interfacial water. It is generally believed that the H in the O–H group of HCOOH can exchange with deuterium oxide (D<sub>2</sub>O), while the H atom in the H–C group cannot exchange with D<sub>2</sub>O at room temperature. Accordingly, we perform in-situ isotope-labeling MS measurements with different substrates, including sodium formate (HCOONa), sodium formate-d (DCOONa) and solvents H<sub>2</sub>O/D<sub>2</sub>O. This ingenious approach eliminates the interference of formic acid, a weak monoprotic acid ionizes according to the Eq. S1. In this way, we accurately track various hydrogen atoms' behavior according to the mass-to-charge ratio ( $m/z$ ) signals of possible intermediate products.

As illustrate in Fig. 4d, the ionic current intensity of  $m/z = 2$  increases rapidly with HCOONa solution addition, indicating the formation of H<sub>2</sub>. More intriguingly, the signals of  $m/z = 2$ ,  $m/z = 3$  and  $m/z = 4$  (H<sub>2</sub>, HD and D<sub>2</sub>) all appear and intensifies either in the case of DCOONa + H<sub>2</sub>O or HCOONa + D<sub>2</sub>O. As for the case of DCOONa + H<sub>2</sub>O, in HD species, D (deuterium) and H are from D atoms in DCOONa and H atoms in H<sub>2</sub>O, respectively. In D<sub>2</sub> species, both D atoms are from DCOONa. In H<sub>2</sub> species, both H atoms are from H<sub>2</sub>O. Contrary to the reaction mechanism in general that the hydrogen atoms in H<sub>2</sub> are only derived from sodium formate. [46–48] A similar experimental phenomenon can be observed in the case of HCOONa + D<sub>2</sub>O. Equally to

sodium formate, water serve as hydrogen source involves in the reaction process through hydrogen bond network. Furthermore, this catalytic process is most likely to follow a new reaction mechanism displayed in Scheme S1. Specifically, interfacial water molecules are dissociated on the catalyst surface, then sequentially to form surface OH\* and hydrogen atom, which then combine with HCOO\* to get H<sub>2</sub> and CO<sub>2</sub> with the assistant of hydrogen bond. Indeed, the transient formation of HCOOH ( $m/z = 46$ ) further confirms the rapid diffusion of protons through extensive hydrogen-bonded network between water and formate (Fig. 4d and Fig. S13).

#### 4. Conclusions

The water-promoted restructured HCOONa-Pd@ANI/C catalyst exhibits extraordinary catalytic performance towards formic acid to hydrogen under ambient conditions. In tandem with PEMFCs, this integrated system reaches a peak power density at 29.81 W·g<sub>Pd</sub><sup>-1</sup>. Simultaneously, a series of elaborate characterizations including AC–HAADF–STEM, *operando* surface-enhanced FT-IR and isotope-labeled in-situ mass spectrometry unveils the underlying mechanism of restructuring process. With water-assisted protons capturing and transferring, sodium formate reduces Pd<sup>2+</sup> to Pd<sup>0</sup>, accompanied with the in-situ formation of ultrafine Pd nanoparticles. Additionally, a new reaction pathway involving water with hydrogen shuttling and exchange is proposed in light of experimental evidence. In a nutshell, our research sheds light on the central roles of interfacial water during the reaction process of FAD and opens up a new paradigm to achieve a continuous conversion of green chemical energy to electricity.

#### CRediT authorship contribution statement

This manuscript includes contributions from all listed authors, who have reviewed and approved the final version of the document.

**Nanxing Gao:** Conceptualization, Data curation, Statistical analyses,

Investigation, Validation, Writing – original draft. **Dongchen Han:** Investigation, Data curation, Statistical analyses. **Tongtong Yang:** Data curation, Statistical analyses. **Qinglei Meng:** Investigation, Validation. **Xian Wang:** Conceptualization, Investigation, Validation, Writing – review & editing. **Changpeng Liu:** Funding acquisition, Project administration. **Junjie Ge:** Conceptualization, Investigation, Writing – review & editing. **Wei Xing:** Conceptualization, Funding acquisition, Investigation, Project administration, Writing – review & editing.

## Declaration of Competing Interest

The authors declare that they have no known competing financial interests or personal relationships that could have appeared to influence the work reported in this paper.

## Data Availability

Data will be made available on request.

## Acknowledgment

The work was supported by the National Natural Science Foundation of China (U22A20396, 22209168), Jilin Province Science and Technology Development Program (YDZJ202202CXJD011, 20210502002ZP).

## Appendix A. Supporting information

Supplementary data associated with this article can be found in the online version at [doi:10.1016/j.apcatb.2023.122913](https://doi.org/10.1016/j.apcatb.2023.122913).

## References

- [1] L. Schlapbach, A. Züttel, Hydrogen-storage materials for mobile applications, *Nature* 414 (2001) 353–358, <https://doi.org/10.1038/35104634>.
- [2] C. Fellay, P.J. Dyson, G. Laurenczy, A viable hydrogen-storage system based on selective formic acid decomposition with a ruthenium catalyst, *Angew. Chem. Int. Ed. Engl.* 47 (2008) 3966–3968, <https://doi.org/10.1002/anie.200800320>.
- [3] Z.L. Wang, J.M. Yan, Y. Ping, H.L. Wang, W.T. Zheng, Q. Jiang, An efficient CoAuPd/C catalyst for hydrogen generation from formic acid at room temperature, *Angew. Chem. Int. Ed. Engl.* 52 (2013) 4406–4409, <https://doi.org/10.1002/anie.201301009>.
- [4] R.I. Amos, F. Heinroth, B. Chan, S. Zheng, B.S. Haynes, C.J. Easton, A.F. Masters, L. Radom, T. Maschmeyer, Hydrogen from formic acid through its selective disproportionation over sodium germanate-a non-transition-metal catalysis system, *Angew. Chem. Int. Ed. Engl.* 53 (2014) 11275–11279, <https://doi.org/10.1002/anie.201405360>.
- [5] J. Eppinger, K.-W. Huang, Formic acid as a hydrogen energy carrier, *ACS Energy Lett.* 2 (2016) 188–195, <https://doi.org/10.1021/acsenenergylett.6b00574>.
- [6] Q.Y. Bi, J.D. Lin, Y.M. Liu, H.Y. He, F.Q. Huang, Y. Cao, Dehydrogenation of formic acid at room temperature: boosting palladium nanoparticle efficiency by coupling with pyridinic-nitrogen-doped carbon, *Angew. Chem. Int. Ed. Engl.* 55 (2016) 11849–11853, <https://doi.org/10.1002/anie.201605961>.
- [7] J. Chen, Q. Ma, Z. Yu, M. Li, S. Dong, Platinum-gold alloy catalyzes the aerobic oxidation of formic acid for hydrogen peroxide synthesis, *Angew. Chem. Int. Ed. Engl.* 61 (2022), e202213930, <https://doi.org/10.1002/ange.202213930>.
- [8] X. Zhou, Y. Huang, W. Xing, C. Liu, J. Liao, T. Lu, High-quality hydrogen from the catalyzed decomposition of formic acid by Pd-Au/C and Pd-Ag/C, *Chem. Commun.* (2008) 3540–3542, <https://doi.org/10.1039/B803661F>.
- [9] Y. Shi, Y. Ji, J. Long, Y. Liang, Y. Liu, Y. Yu, J. Xiao, B. Zhang, Unveiling hydrocerussite as an electrochemically stable active phase for efficient carbon dioxide electroreduction to formate, *Nat. Commun.* 11 (2020) 3415, <https://doi.org/10.1038/s41467-020-17120-z>.
- [10] Q. Sun, B.W.J. Chen, N. Wang, Q. He, A. Chang, C.M. Yang, H. Asakura, T. Tanaka, M.J. Hulsey, C.H. Wang, J. Yu, N. Yan, Zeolite-encaged Pd-Mn nanocatalysts for CO<sub>2</sub> hydrogenation and formic acid dehydrogenation, *Angew. Chem. Int. Ed. Engl.* 59 (2020) 20183–20191, <https://doi.org/10.1002/anie.202008962>.
- [11] C. Wang, X. Chen, M. Qi, J. Wu, G. Gözaydın, N. Yan, H. Zhong, F. Jin, Room temperature, near-quantitative conversion of glucose into formic acid, *Green. Chem.* 21 (2019) 6089–6096, <https://doi.org/10.1039/C9GC02201E>.
- [12] Z. Zhang, L. Zhang, S. Yao, X. Song, W. Huang, M.J. Hulsey, N. Yan, Support-dependent rate-determining step of CO<sub>2</sub> hydrogenation to formic acid on metal oxide supported Pd catalysts, *J. Catal.* 376 (2019) 57–67, <https://doi.org/10.1016/j.jcat.2019.06.048>.
- [13] B. Loges, A. Boddien, H. Junge, M. Beller, Controlled generation of hydrogen from formic acid amine adducts at room temperature and application in H<sub>2</sub>/O<sub>2</sub> fuel cells, *Angew. Chem. Int. Ed. Engl.* 47 (2008) 3962–3965, <https://doi.org/10.1002/anie.200705972>.
- [14] X. Zhou, Y. Huang, C. Liu, J. Liao, T. Lu, W. Xing, Available hydrogen from formic acid decomposed by rare earth elements promoted Pd-Au/C catalysts at low temperature, *ChemSusChem* 3 (2010) 1379–1382, <https://doi.org/10.1002/cssc.201000199>.
- [15] Q. Lv, L. Feng, C. Hu, C. Liu, W. Xing, High-quality hydrogen generated from formic acid triggered by in situ prepared Pd/C catalyst for fuel cells, *Catal. Sci. Technol.* 5 (2015) 2581–2584, <https://doi.org/10.1039/C5CY00245A>.
- [16] M. Czaun, J. Kothandaraman, A. Goepfert, B. Yang, S. Greenberg, R.B. May, G. A. Olah, G.K.S. Prakash, Iridium-catalyzed continuous hydrogen generation from formic acid and its subsequent utilization in a fuel cell: toward a carbon neutral chemical energy storage, *ACS Catal.* 6 (2016) 7475–7484, <https://doi.org/10.1021/acscatal.6b01605>.
- [17] J.S. Yoo, F. Abild-Pedersen, J.K. Nørskov, F. Studt, Theoretical analysis of transition-metal catalysts for formic acid decomposition, *ACS Catal.* 4 (2014) 1226–1233, <https://doi.org/10.1021/cs400664z>.
- [18] Y.H. Wang, S. Zheng, W.M. Yang, R.Y. Zhou, Q.F. He, P. Radjenovic, J.C. Dong, S. Li, J. Zheng, Z.L. Yang, G. Attard, F. Pan, Z.Q. Tian, J.F. Li, In situ Raman spectroscopy reveals the structure and dissociation of interfacial water, *Nature* 600 (2021) 81–85, <https://doi.org/10.1038/s41586-021-04068-z>.
- [19] Z. Liu, E. Huang, I. Orozco, W. Liao, R.M. Palomino, N. Rui, T. Duchon, S. Nemsak, D.C. Grinter, M. Mahapatra, P. Liu, J.A. Rodriguez, S.D. Senanayake, Water-promoted interfacial pathways in methane oxidation to methanol on a CeO<sub>2</sub>-Cu<sub>2</sub>O catalyst, *Science* 368 (2020) 513–517, <https://doi.org/10.1126/science.aba5005>.
- [20] L.F. Shen, B.A. Lu, Y.Y. Li, J. Liu, Z.C. Huang-Fu, H. Peng, J.Y. Ye, X.M. Qu, J. M. Zhang, G. Li, W.B. Cai, Y.X. Jiang, S.G. Sun, Interfacial structure of water as a new descriptor of the hydrogen evolution reaction, *Angew. Chem. Int. Ed. Engl.* 59 (2020) 22397–22402, <https://doi.org/10.1002/anie.202007567>.
- [21] K. Zhao, X. Chang, H.S. Su, Y. Nie, Q. Lu, B. Xu, Enhancing hydrogen oxidation and evolution kinetics by tuning the interfacial hydrogen-bonding environment on functionalized platinum surfaces, *Angew. Chem. Int. Ed. Engl.* 61 (2022), e202207197, <https://doi.org/10.1002/anie.202207197>.
- [22] N. Agmon, The Grotthuss mechanism, *Chem. Phys. Lett.* 244 (1995) 456–462, [https://doi.org/10.1016/0009-2614\(95\)00905-J](https://doi.org/10.1016/0009-2614(95)00905-J).
- [23] J.J. Velasco-Velez, C.H. Wu, T.A. Pascal, L.F. Wan, J. Guo, D. Prendergast, M. Salmeron, Interfacial water. The structure of interfacial water on gold electrodes studied by x-ray absorption spectroscopy, *Science* 346 (2014) 831–834, <https://doi.org/10.1126/science.1259437>.
- [24] X. Ma, Y. Shi, J. Liu, X. Li, X. Cui, S. Tan, J. Zhao, B. Wang, Hydrogen-bond network promotes water splitting on the TiO<sub>2</sub> surface, *J. Am. Chem. Soc.* 144 (2022) 13565–13573, <https://doi.org/10.1021/jacs.2c03690>.
- [25] M. Karuppannan, Y. Kim, S. Gok, E. Lee, J.Y. Hwang, J.-H. Jang, Y.-H. Cho, T. Lim, Y.-E. Sung, O.J. Kwon, A highly durable carbon-nanofiber-supported Pt-C core-shell cathode catalyst for ultra-low Pt loading proton exchange membrane fuel cells: facile carbon encapsulation, *Energy Environ. Sci.* 12 (2019) 2820–2829, <https://doi.org/10.1039/C9EE01000A>.
- [26] S. Chen, Z. Wei, X. Qi, L. Dong, Y.G. Guo, L. Wan, Z. Shao, L. Li, Nanostructured polyaniline-decorated Pt/C@PANI core-shell catalyst with enhanced durability and activity, *J. Am. Chem. Soc.* 134 (2012) 13252–13255, <https://doi.org/10.1021/ja306501x>.
- [27] J.X. Feng, S.Y. Tong, Y.X. Tong, G.R. Li, Pt-like hydrogen evolution electrocatalysis on PANI/CoP hybrid nanowires by weakening the shackles of hydrogen ions on the surfaces of catalysts, *J. Am. Chem. Soc.* 140 (2018) 5118–5126, <https://doi.org/10.1021/jacs.7b12968>.
- [28] J. Ryu, C.B. Park, Synthesis of diphenylalanine/polyaniline core/shell conducting nanowires by peptide self-assembly, *Angew. Chem. Int. Ed. Engl.* 48 (2009) 4820–4823, <https://doi.org/10.1002/anie.200900668>.
- [29] T.W. Song, C. Xu, Z.T. Sheng, H.K. Yan, L. Tong, J. Liu, W.J. Zeng, L.J. Zuo, P. Yin, M. Zuo, S.Q. Chu, P. Chen, H.W. Liang, Small molecule-assisted synthesis of carbon supported platinum intermetallic fuel cell catalysts, *Nat. Commun.* 13 (2022) 6521, <https://doi.org/10.1038/s41467-022-34037-7>.
- [30] T. Kuribara, M. Nakajima, T. Nemoto, A visible-light activated secondary phosphine oxide ligand enabling Pd-catalyzed radical cross-couplings, *Nat. Commun.* 13 (2022) 4052, <https://doi.org/10.1038/s41467-022-31613-9>.
- [31] L. Espinosa-Alonso, K.P. de Jong, B.M. Weckhuysen, A UV-Vis micro-spectroscopic study to rationalize the influence of Cl<sup>-</sup>(aq) on the formation of different Pd macro-distributions on gamma-Al<sub>2</sub>O<sub>3</sub> catalyst bodies, *Phys. Chem. Chem. Phys.* 12 (2010) 97–107, <https://doi.org/10.1039/B915753K>.
- [32] N.X. Gao, R.P. Ma, X. Wang, Z. Jin, S. Hou, W.L. Xu, Q.L. Meng, J.J. Ge, C.P. Liu, W. Xing, Activating the Pd-based catalysts via tailoring reaction interface towards formic acid dehydrogenation, *Int. J. Hydrog. Energy* 45 (2020) 17575–17582, <https://doi.org/10.1016/j.ijhydene.2020.04.289>.
- [33] Q. Wang, N. Tsumori, M. Kitta, Q. Xu, Fast dehydrogenation of formic acid over palladium nanoparticles immobilized in nitrogen-doped hierarchically porous carbon, *ACS Catal.* 8 (2018) 12041–12045, <https://doi.org/10.1021/acscatal.8b03444>.
- [34] D.Y. Chung, S.W. Jun, G. Yoon, H. Kim, J.M. Yoo, K.S. Lee, T. Kim, H. Shin, A. K. Sinha, S.G. Kwon, K. Kang, T. Hyeon, Y.E. Sung, Large-scale synthesis of carbon-shell-coated FeP nanoparticles for robust hydrogen evolution reaction electrocatalysis, *J. Am. Chem. Soc.* 139 (2017) 6669–6674, <https://doi.org/10.1021/jacs.7b01530>.
- [35] J. Graciani, K. Mudiyansele, F. Xu, A.E. Baber, J. Evans, S.D. Senanayake, D. J. Stacchiola, P. Liu, J. Hrbek, J. Hernandez Sanz, J.A. Rodriguez, Catalysis Highly active copper-ceria and copper-ceria-titania catalysts for methanol synthesis from CO<sub>2</sub>, *Science* 345 (2014) 546–550, <https://doi.org/10.1126/science.1253057>.



- [36] K. Jiang, K. Xu, S. Zou, W.B. Cai, B-doped Pd catalyst: boosting room-temperature hydrogen production from formic acid-formate solutions, *J. Am. Chem. Soc.* 136 (2014) 4861–4864, <https://doi.org/10.1021/ja5008917>.
- [37] K. Koichumanova, K.B. Sai Sankar Gupta, L. Lefferts, B.L. Mojet, K. Seshan, An in situ ATR-IR spectroscopy study of aluminas under aqueous phase reforming conditions, *Phys. Chem. Chem. Phys.* 17 (2015) 23795–23804, <https://doi.org/10.1039/C5CP02168E>.
- [38] J. Chen, Z. Li, X. Wang, X. Sang, S. Zheng, S. Liu, B. Yang, Q. Zhang, L. Lei, L. Dai, Y. Hou, Promoting CO<sub>2</sub> electroreduction kinetics on atomically dispersed monovalent Zn(I) sites by rationally engineering proton-feeding centers, *Angew. Chem. Int. Ed. Engl.* 61 (2022), e202111683, <https://doi.org/10.1002/anie.202111683>.
- [39] W. Zhang, Q. Qin, L. Dai, R. Qin, X. Zhao, X. Chen, D. Ou, J. Chen, T.T. Chuong, B. Wu, N. Zheng, Electrochemical reduction of carbon dioxide to methanol on hierarchical Pd/SnO<sub>2</sub> nanosheets with abundant Pd-O-Sn interfaces, *Angew. Chem. Int. Ed. Engl.* 57 (2018) 9475–9479, <https://doi.org/10.1002/anie.201804142>.
- [40] T. Hou, Q. Luo, Q. Li, H. Zu, P. Cui, S. Chen, Y. Lin, J. Chen, X. Zheng, W. Zhu, S. Liang, J. Yang, L. Wang, Modulating oxygen coverage of Ti<sub>3</sub>C<sub>2</sub>T<sub>x</sub> MXenes to boost catalytic activity for HCOOH dehydrogenation, *Nat. Commun.* 11 (2020) 4251, <https://doi.org/10.1038/s41467-020-18091-7>.
- [41] J.D. Yi, R. Xie, Z.L. Xie, G.L. Chai, T.F. Liu, R.P. Chen, Y.B. Huang, R. Cao, Highly selective CO<sub>2</sub> electroreduction to CH<sub>4</sub> by in situ generated Cu<sub>2</sub>O single-type sites on a conductive MOF: stabilizing key intermediates with hydrogen bonding, *Angew. Chem. Int. Ed. Engl.* 59 (2020) 23641–23648, <https://doi.org/10.1002/anie.202010601>.
- [42] J.Y. Wang, H.X. Zhang, K. Jiang, W.B. Cai, From HCOOH to CO at Pd electrodes: a surface-enhanced infrared spectroscopy study, *J. Am. Chem. Soc.* 133 (2011) 14876–14879, <https://doi.org/10.1021/ja205747j>.
- [43] P. Liu, Z. Huang, X. Gao, X. Hong, J. Zhu, G. Wang, Y. Wu, J. Zeng, X. Zheng, Synergy between palladium single atoms and nanoparticles via hydrogen spillover for enhancing CO<sub>2</sub> Photoreduction to CH<sub>4</sub>, *Adv. Mater.* 34 (2022), e2200057, <https://doi.org/10.1002/adma.202200057>.
- [44] J.R. McBride, K.C. Hass, W.H. Weber, Resonance-Raman and lattice-dynamics studies of single-crystal PdO, *Phys. Rev. B Condens Matter* 44 (1991) 5016–5028, <https://doi.org/10.1103/PhysRevB.44.5016>.
- [45] H. Zhang, C. Wang, H.L. Sun, G. Fu, S. Chen, Y.J. Zhang, B.H. Chen, J.R. Anema, Z. L. Yang, J.F. Li, Z.Q. Tian, In situ dynamic tracking of heterogeneous nanocatalytic processes by shell-isolated nanoparticle-enhanced Raman spectroscopy, *Nat. Commun.* 8 (2017) 15447, <https://doi.org/10.1038/ncomms15447>.
- [46] Q.Y. Bi, J.D. Lin, Y.M. Liu, X.L. Du, J.Q. Wang, H.Y. He, Y. Cao, An aqueous rechargeable formate-based hydrogen battery driven by heterogeneous Pd catalysis, *Angew. Chem. Int. Ed. Engl.* 53 (2014) 13583–13587, <https://doi.org/10.1002/anie.201409500>.
- [47] W.J. Lee, Y.J. Hwang, J. Kim, H. Jeong, C.W. Yoon, Pd<sup>2+</sup> -/thways for C-H activation of formate, *Chemphyschem* 20 (2019) 1382–1391, <https://doi.org/10.1002/cphc.201801088>.
- [48] B.W.J. Chen, S. Bhandari, M. Mavrikakis, Role of hydrogen-bonded bimolecular formic acid–formate complexes for formic acid decomposition on copper: a combined first-principles and microkinetic modeling study, *ACS Catal.* 11 (2021) 4349–4361, <https://doi.org/10.1021/acscatal.0c05695>.